ICAS 2020 SHANGHAI
International Council of the Aeronautical Sciences
32nd Congress of the International Council of the Aeronautical Sciences
September 6-10, 2021
Pudong Shangri-La, Shanghai, China

AERODYNAMIC ANALYSIS OF A FULL MODEL WITH ADAPTIVE ELASTO-FLEXIBLE MEMBRANE WINGS

Jonathan Pflüger[1], Kevin Hirschmann[1] & Christian Breitsamter[1]

[1]Chair of Aerodynamics and Fluid Mechanics, Technical University of Munich, Boltzmannstr. 15, 85748 Garching, Germany,

Abstract

Unmanned and micro aerial vehicles operate under a variety of flight conditions. The application of morphing wings for these aircraft offer the possibility to adapt the aerodynamics to different flight stages. The investigated model consists of two deformable wing structures, which are covered by an elastic membrane. The concept enables wing folding over a wide range and it allows the wing to adapt to changing aerodynamic loads. The present study focuses on the fluid-structure-interaction simulations of the elasto-flexible membrane and the surrounding fluid at a Reynolds number of 264000. For validation, the results of the numerical simulations are compared to experimental data. Hereby, the membrane deformation, the aerodynamic coefficients and the flow field in the wake of the wing are examined. The numerical results of the highly swept wing show good agreement with the measurement data. With a more extended wing, the lift is overpredicted at small angles of attack and underpredicted at high angles of attack. The simulations generate larger flow separation areas than can be observed in the wind tunnel.

Keywords: Morphing Wing, Flexible Wing Surface, Morphing Camber, Fluid-Structure-Interaction Simulation

1. Introduction

In recent years, the number of unmanned aerial vehicles (UAV) and micro aerial vehicles (MAV) operating worldwide has increased significantly. In addition, the field of application for those aircraft is becoming wider and more manifold. The main goal is to design cheap and expandable platforms for surveillance and data collection in areas, where large aircraft are not practical. For example, they can help mapping the extent of chemical and radiation spills or viral outbreaks [1]. Further civil applications include search and rescue operations, traffic and news coverage, and crop or wildlife monitoring [1]. The different flight conditions lead to numerous design and construction requirements.

The morphing wing technology can be a solution to this problem, as it allows, in a first approach, the aircraft shape to be adapted for optimal performance at various flight stages. The benefits of morphing wings are accompanied by the complicated technical realization concerning the structural design, actuators, materials and the flight controls. The aerodynamic improvements compete against the penalties by additional structures, the increased weight and the energy consumption [2, 3].

The second approach of morphing technologies is the use of deformable or elastic materials as aerodynamic surfaces. Especially, small and lightweight vehicles like MAVs are exposed to a highly unsteady flight environment. The operation at ground level with a lot of obstacles like buildings, trees, birds and other aerial vehicle involves gusty wind conditions and requires high agility. In turbulent conditions, the passive morphing of flexible wing surfaces can help to reduce loads and improve the stability [4]. An additional feature is the superior stall characteristics, because the shape of the airfoil passively adapts to the inflow at high angles of attack. Song et al. [5] analyzed membrane wings of varying aspect ratio, compliancy, and pre-stress values. Piquee et al. [6] investigated the capacity of a flexible membrane to adapt itself to the incoming flow by experimental and numerical investigations. The overall scientific aim of the project is the extension and deepening of the understanding of concepts for morphing aircraft. The concept for the elasto-flexible morphing wing at the Technical University of Munich (TUM) was originally developed by Beguin et al. [7]. The investigated morphing

wing is part of a common research project with the Beihang University [8, 9]. Both project partners investigate morphing wind tunnel models in their facilities.

2. The Elasto-Flexible Morphing Wing

2.1 Description of the Concept

In nature, wings consisting of thin, elastic skin membranes are used by several species. A common example is the bat, whose flight is analyzed in detail by Breuer [11]. Particularly interesting about bats is that they have a high degree of articulation in the wing and the lifting surface is composed of a highly elastic skin membrane. Hence, they can change their wing planform and airfoil to perform various flight maneuvers. The bio inspired concept for the membrane wing of the present investigations is oriented to the "wing design" of the Pterosaurs [12]. The structure of their wings consists of a rigid skeleton, while a thin, elastic skin forms the aerodynamic wing surface.

Figure 1 illustrates the concept of the investigated configuration within this paper. The position of the leading-edge (LE) spar actively defines the shape of the wing by the folding angle Ω. The wing half span s, the aspect ratio AR and the quarter line sweep angle $\Phi_{(1/4)}$ are actively adjusted. Both wings can be actuated individually, which enables asymmetric wing positions. The elastic membrane serves as the actual aerodynamic surface and guarantees a smooth and continuous wing surface during the inclination of the wings.

In addition, the elasticity of the membrane allows the airfoil to passively adapt to aerodynamic loads. This mechanism changes primarily the camber and the thickness of the airfoil. The membrane is mounted with a certain pre-stress, which is calculated in the mechanical-pre-stress module, shown in section 4.2. For a predecessor wind tunnel model, the influence of the pre-stress at different flow velocities and wing positions was already experimentally investigated in detail by Beguin and Breitsamter [10].

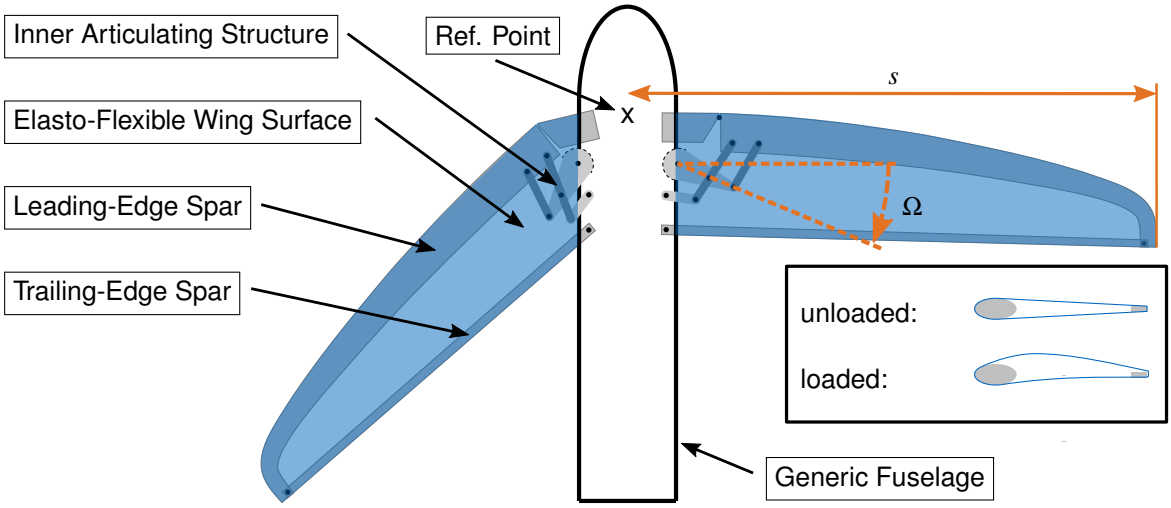

Figure 1 – Illustration of the morphing wing concept.

2.2 Model Design

The two individually foldable wings of the model provide an aspect ratio of $5 \leq AR \leq 10$ and a quarter-chord sweep angle of $5° \leq \Phi_{(1/4)} \leq 45°$. An elasto-flexible membrane represents the aerodynamic wing surface.

Two stepper motors in combination with a folding mechanism inside the wing actuate the wings. The position of the wing is determined by the folding angle Ω, see Fig. 1. Figure 2 shows the right side of the model and the schematic cross section of the wing with its components, including the spanned membrane in blue. The main components of the wing structure are given by the elliptical LE spar and the rectangular trailing-edge (TE) spar. The LE has an elliptical planform and tapers in spanwise direction. The TE spar is straight, because its length must adapt to the current wing position in order

to provide a rigid closed frame to stretch the membrane.
The material of the membrane is an elasto-flexible commercial polyurethane (PU) foil provided by the PU-manufacturer Pharetra (Pharetra Textile Kunststoffanwendung GmbH & Co. KG). The membrane has a thickness of $t = 65\ \mu m$ and an isotropic stiffness with a Young's modulus of about $E_{mem} \approx 1.03\ MPa$. The high elasticity produces a measurable surface deformation by the expected aerodynamic loads. The membrane is welded along the LE, pulled over the wing and fixed under the fuselage cover by a wire.
The deformation of the wing surface depends strongly on the pre-stress of the membrane. The pre-stress can be adjusted by shifting the attachment of the TE at the fuselage in axial direction. For the measurements and the simulations within this paper, the wing root chord is fixed to $c_r = 0.14\ m$.

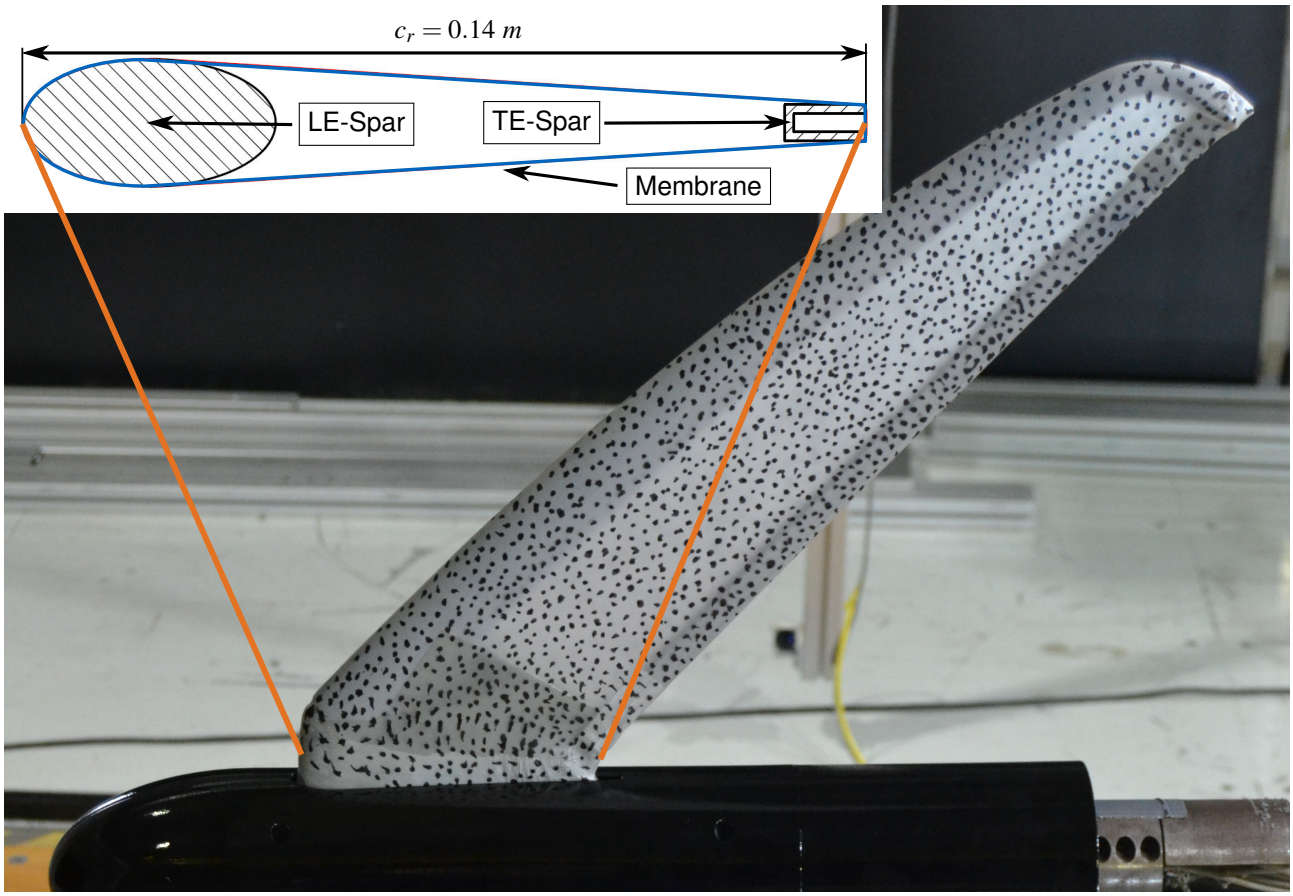

Figure 2 – The mounted elastic membrane on the left wing structure, the fuselage and the schematic airfoil cross section.

3. Experimental Methods

The experiments with the membrane wing are conducted in the Göttingen-type, closed-loop, low-speed wind tunnel W/T A of the Chair of Aerodynamics and Fluid Mechanics at the Technical University of Munich. The dimensions of the open test section are $1.8\ m \times 2.4\ m \times 4.8\ m$ ($height \times width \times length$). The W/T has a turbulence level below $0.4\ \%$ and a flow non-uniformity of less then $0.6\ \%$ of the freestream velocity. The model is mounted on a rear sting of a three-axis support. The measurements are performed at a Reynolds number, based on the wing root chord, of $Re_\infty = 264000$ and a Mach number of $Ma_\infty = 0.09$, which corresponds to a dynamic pressure of $q_\infty = 530\ Pa$. The measurements comprise angles of attack of $-10° \leq \alpha \leq 30°$. All measurements are conducted for three symmetric wing positions: "The High Aspect Ratio Configuration" (HAC, $\Omega = 23°$), the "Intermediate Configuration" (INC, $\Omega = 43°$) and the "Highly Swept Configuration" (HSC, $\Omega = 63°$).
The forces and moments are measured with an internal six-component strain-gauge balance, which is mounted between the rear part of the model and the support. The sampling frequency for the measurements is set to $f_{meas,force} = 800\ Hz$ and a Butterworth filter of $200Hz$ is applied. The forces

and moments are averaged over a total acquisition time of $t_{meas} = 5\ s$. The aerodynamic coefficients are normalized by the current wing surface and the moment coefficient additionally by the wing root. The reference point for the moment coefficients is located on the longitudinal axis on a level with the intersection of LE and fuselage, marked by the black cross in Fig. 1.
The flow-field data in the wake region is obtained by the stereo particle image velocimetry (2D/Stereo-PIV) method. For the comparison of the cross-flow characteristics behind different wing positions, the PIV measurements are conducted on slices perpendicular to the inflow and at a constant distance of $1.5 \times c_r$ downstream of the wing tip. The PIV setup is shown in Fig. 3. Seeding particles with a diameter of $d \approx 1\ \mu m$ are inserted into the flow for the PIV measurements. Each camera records two raw pictures per measurement with a time offset of $\Delta t \approx 10\ \mu s$. A time series of 400 shots with a sampling rate of $f_{meas,PIV} = 15\ Hz$ is recorded for each measurement plane. The mean and root-mean-square values of the velocity components are determined from the velocity fields of the 400 image pairs. The uncertainties of the single velocity components are calculated inside the post processing software DaVis by means of a method developed by Wieneke [13]. In the most critical area, which is given by the location of the wing tip vortex, uncertainties of less than one percent of the inflow velocity occur for the axial flow velocity component $(u_{err} < 0.01 \cdot U_\infty)$. A more detailed report about the flow field measurements is presented by Pflueger and Breitsamter [14].
The deformation of the aerodynamically deformed membrane is measured by a digital image correlation system (DIC). Figure 4 shows the DIC setup on the bottom side of the wing. The same system is mounted on the top side, which results in four cameras to measure the deformation on both wing sides. The complementary metal oxide semiconductor (CMOS) cameras are placed outside the W/T test section with an angle between the respective optical axes of approximately $\beta = 40°$. The cameras have a maximum frame rate of $10\ Hz$ and a resolution of 1944×2592 pixels, which, in conjunction with the imaging optics (Pentax 16mm CCTV lenses), provide a spatial resolution of $0.34\ mm$ per pixel. For this series of experiments, the deformation of the membrane is recorded with a single snapshot for an exposure time of $0.18\ s$. By using a test object, which is moved in z-direction in controlled manner, the uncertainty of the DIC system for out-of-plane displacements is determined to be less than $\Delta z = 0.5\ mm\ (\Delta z/c_r = 0.0036)$. The measurement setup is explained in more detail by Pflueger and Breitsamter [15].

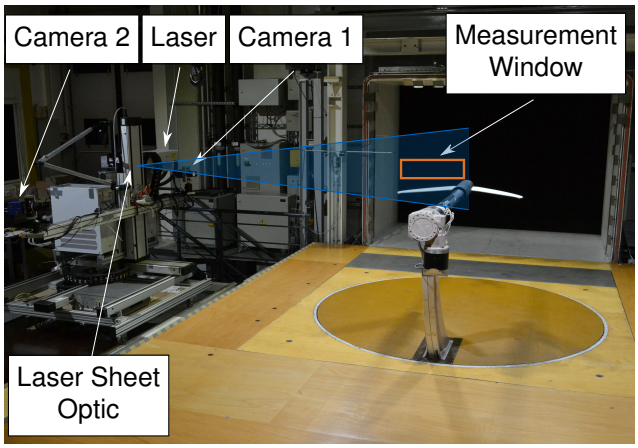

Figure 3 – Back view of the experimental setup for the PIV measurements.

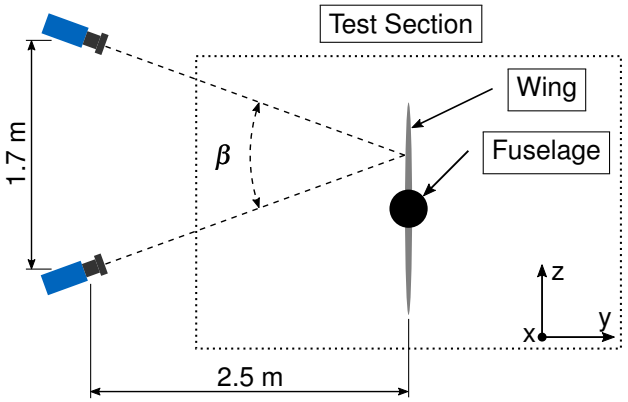

Figure 4 – Schematic front view of the DIC setup for the deformation measurements.

4. Numerical Methods

The geometry of the numerical model conforms with the W/T model except at the TE, at the wing tip and at the intersection between wing and fuselage, where the numerical model is simplified. In addition, the rear sting support is neglected. Overall nine cases are simulated: Three angles of attack $\alpha = [5°,\ 10°,\ 15°]$, for the three different folding angles $\Omega = [23°,\ 43°,\ 63°]$. The simulations run on 224 cores at the Linux-Cluster of the Leibnitz Rechenzentrum [16]. The total simulation of 140

timesteps last about 18 hours, depending on the angle of attack.

4.1 FSI Setup

The two-way fluid-structure-interaction (FSI) simulations are performed with the ANSYS System-Coupling (SC) Toolbox [17]. ANSYS Mechanical solves the structural mechanic part, while ANSYS Fluent solves the fluid mechanic part. Figure 5 shows the SC setup, which consists of the pre-stress-mechanical, the FSI-mechanical and the FSI-fluid module. The SC toolbox controls the data transfer between the interfaces of the FSI-modules. The membranes on the top and the bottom side of the wing are defined as SC-interfaces. The FSI-fluid module provides the forces, which are acting on the membrane surface, while the FSI-mechanical module returns the resulting displacements. For the SC simulations, a timestep of $t_{SC} = 0.01\ s$ is applied and a maximum of five system coupling iterations per time step is set. Because of the fluid mesh is much larger, the mechanical solver runs with 10 cores and the fluid solver with 214 cores.
The pre-stress-mechanical module calculates the initial stresses on the membrane by a backward translation and rotation of the TE. The FSI-modules load the deformed mesh and the initial stress on the membrane.

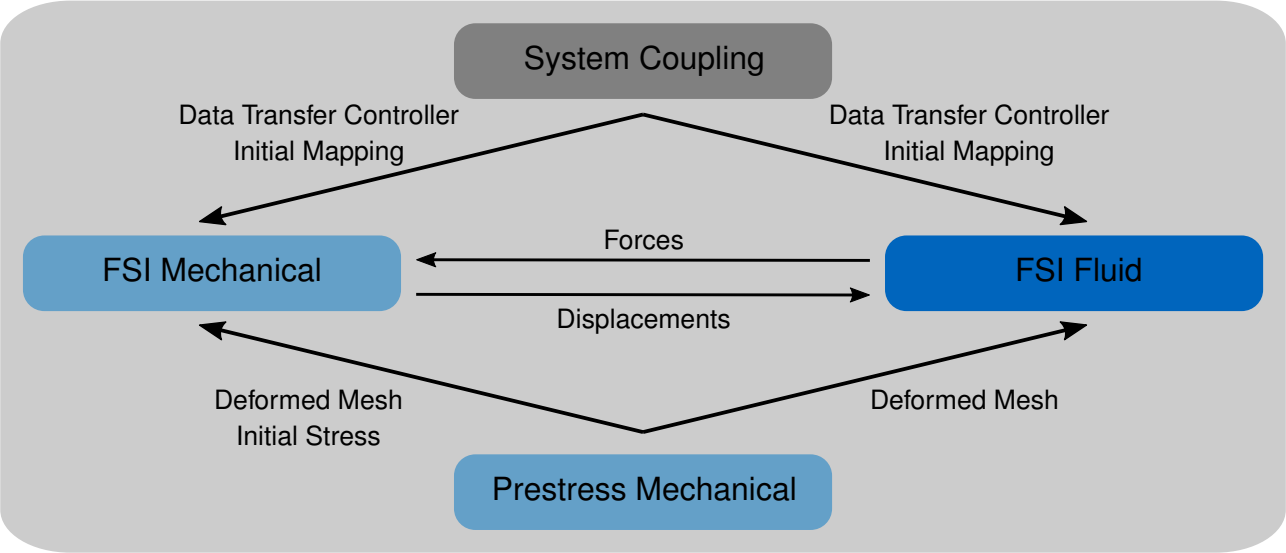

Figure 5 – Fluid-structure-interaction simulation setup.

4.2 Mechanical Solver Setup

The structural mesh consists of 35000 Elements and is subdivided into the LE-spar, the TE-spar and the upper and the lower membrane, see Fig. 6. All wing spars must be modeled as 3D flexible bodies, even though their deformations are negligible. The volume mesh is created to consume as little resources as possible, for instances by using linear elements and a low internal resolution. The surface mesh of the spars is matching to the mesh of the membranes to ensure an accurate contact detection and calculation. The mesh for the membranes consists of quadratic shell elements with a thickness of only one element. At the LE, the size of the elements is reduced in order to resolve the local curvature, while at the TE, the elements are enlarged to prevent the membrane from tearing during the pre-stress simulations.
The LE-spar is locked in position, while the TE-spar moves only during the pre-stress calculation. The membrane is spanned over both spars by fixations at the apex of the LE and at the rear side of the TE. In addition, a frictionless contact condition between the membrane and the surfaces of the LE- and TE-spars is applied. At the wing tip and root, the membrane is held in spanwise direction. The initial numerical membrane cut is larger than the underlying structure, in order that the contact conditions between membrane and spars are setup correctly. Therefore, the membrane must first

touch the spars before being stretched any further.
In the analysis settings, a sparse direct equation solver with nonlinear effects is chosen. Weak springs are deactivated and large deflections are activated. The energy dissipation ratio is set to 0.0001 and to shorten the calculation time, unnecessary nonlinear computations are deactivated for LE and TE spars. Thermal stress considerations are neglected for the membrane as well as for the structure. The LE and TE are defined as steel, while the material of the membrane is designed to represent the PU foil of the W/T model. At first, the simulations showed an unstable behavior for the membrane thickness of the experiments $t_{exp} = 0.065\ mm$. Therefore, for all presented simulations, the thickness was increased to $t_{sim} = 1\ mm$. For a first parameter study, this adaptation is balanced by an adjustment of the initial Young's modulus E_{sim} via a ratio of the thicknesses t and the mean stresses σ_{mean} like in the following equation:

$$E_{sim} = E_{exp} \frac{t_{exp}}{t_{sim}} \frac{\sigma_{exp,mean}}{\sigma_{sim,mean}} \tag{1}$$

This assumption is a strong simplification, thus two test simulations with a 2D geometry and a test-pressure were run, one with the original properties, the second with the adapted properties. The deformation at both cases completely agree. The Young's modulus controls the global pre-stress of the membrane, while the backward translation and rotation of the TE make sure that the membrane is attached and they define the pre-stress distribution between wing root and wing tip. Table 1 specifies the rotation angle and the translation distance for all three configurations. The isotropic Young's modulus of the membrane is adjusted by an extensive parameter study, so that the calculated membrane deformation matches the deformation measured during the W/T tests. For the three configurations, the measurements at an angle of attack of $\alpha = 10°$ serve as reference cases. The Young's modulus is set to $E_{sim} = 0.675\ MPa$ for all three configurations, which corresponds to an experimental value of $E_{exp} \approx 10\ MPa$. The pre-stress is adjusted for each configuration individually, but held constant over all angles of attack. During the pre-stress calculations, the time step is set to $\Delta t = 0.2\ s$ and the calculation time to $1\ s$.

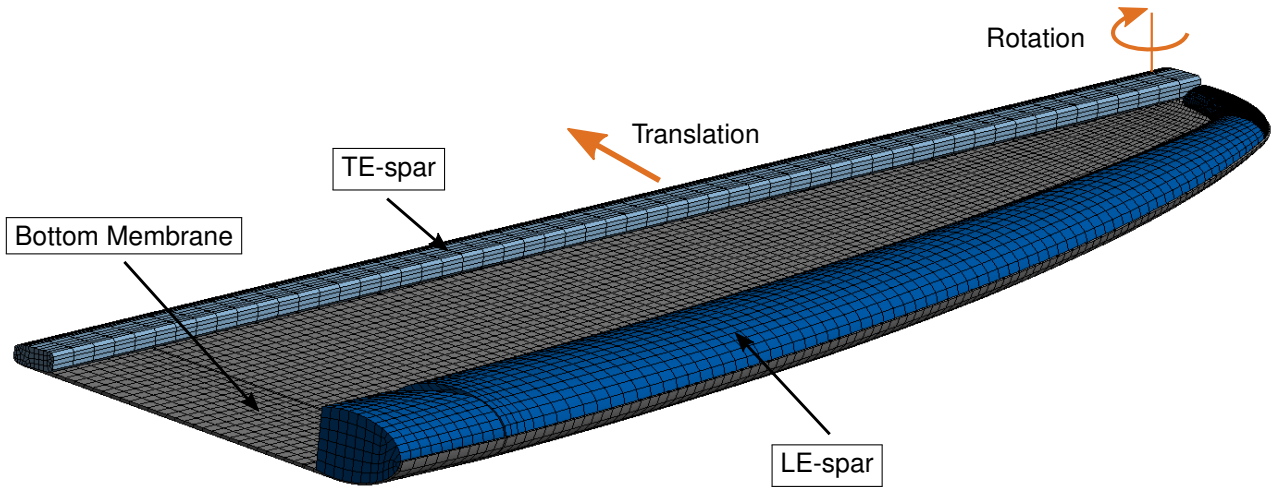

Figure 6 – Mesh of the mechanical structure of the HAC without the upper membrane.

4.3 Fluid Solver Setup

The mesh generation of the fluid domain is performed with the ANSYS Mesher. The fluid mesh of the half model consists of approximately 20 million elements, of which 10 million are located in the refinement zone in the wake behind the wing, see Fig. 7. A detailed mesh convergence study was carried out in a previous student thesis, which results in the current mesh. The maximum element size of the surface mesh at the LE is set to $1\ mm$, at the TE and tip to $0.5\ mm$ and on the rest of the wing to $1.5\ mm$. For $y^+ < 1$, the initial layer height is set to $\Delta n = 0.01\ mm$ and the number of

Table 1 – Geometric parameters for the calculation of the pre-stress.

Configuration	Rotation angle [°]	Translation distance [mm]
HAC	1	10
INT	1.2	9
HSC	0	12

prism-layers to 25. The refinement zone is designed to cover the wake of the wing until $1.5 \times c_r$ behind the wing tip. There, the maximum element size is limited to $2.5\ mm$. To allow the deformation of the membrane, a dynamic mesh with only diffusion based smoothing is used for the fluid domain. The diffusion coefficient is set to 3.
Figure 8 shows the fluid domain with its boundary conditions. Depending on the angle of attack, the rectangular fluid domain is rotated in relation to the model such that the inflow is always perpendicular to the inlet. The inlet is set to pressure-inlet, the symmetry plane to symmetry and the outlet to pressure-outlet. The remaining outer boundary conditions are defined as free slip-walls. The fairing, the membrane and the wing tip are specified as no-slip walls. To avoid critical loads on the membrane in the mechanical module a pressure ramp over $t_{Ramp} = 0.2\ s$ is applied at the inlet. The fluid domain is initialized with $U_\infty = 10\ m/s$, then the corresponding gauge pressure at the inlet rises leading to an operating velocity of $U_\infty = 30\ m/s$.
In ANSYS Fluent, the compressible, unsteady Reynolds-averaged Navier-Stokes equations (URANS) are solved. A pressure-based solver with an active pressure-velocity coupling and a first order implicit transient formulation is chosen. The turbulence modeling is achieved by the k-ω-SST model. After 100 time steps with $\Delta t = 0.01\ s$, another 40 time steps with $\Delta t = 0.005\ s$ are calculated. In order to demonstrate the convergence behavior, Fig. 9 shows the lift coefficient of the HSC as a function of time for three angles of attack. At $\alpha = [5°,\ 10°]$, the coefficients converged to a certain value, while at higher angles of attack no more convergence is reached due to unsteady flow phenomena. Therefore, the coefficients are averaged over the last 40 time steps.

5. Comparison of Experimental and Numerical Results

The presented fluid-structure-interaction simulations complement the wind tunnel measurements. From the experiments, the deformation of the membrane, the aerodynamic coefficients and the velocity field on slices behind the wing are available for comparison. In the following sections, the experimental results are compared to the numerical simulations.

5.1 Membrane Deformation

The validation of the numerical simulations starts with the comparison of the deformation of the membrane. Due to the increased thickness of the membrane in the simulations, the mechanical properties are adjusted. The Young's modulus is set to $E_{sim} = 0.675\ MPa$ for all three configurations. The pre-stress is adjusted for each configuration individually by a translation and rotation of the TE. The pre-stress of one configuration is kept constant over all angles of attack. The deformations in the experiment and the numerical simulation are compared exemplarily at a spanwise position of $y = 150\ mm$, which corresponds to $y/s = 0.25$ for the HAC and to $y/s = 0.36$ for the HSC. Figure 10 and Fig. 11 show the airfoil section of the wing at $U_\infty = 30\ m/s$ and $\alpha = 5°,\ 10°$ for the HAC and HSC, respectively. The orange contour represents the membrane without inflow. The solid lines represent the experimental data and the dashed lines show the numerical results.
At $\alpha = 10°$, the experimentally and numerically obtained deformations on the top and bottom side of the HAC match well, while at $\alpha = 5°$ the top side of the numerical model is too much deformed. For

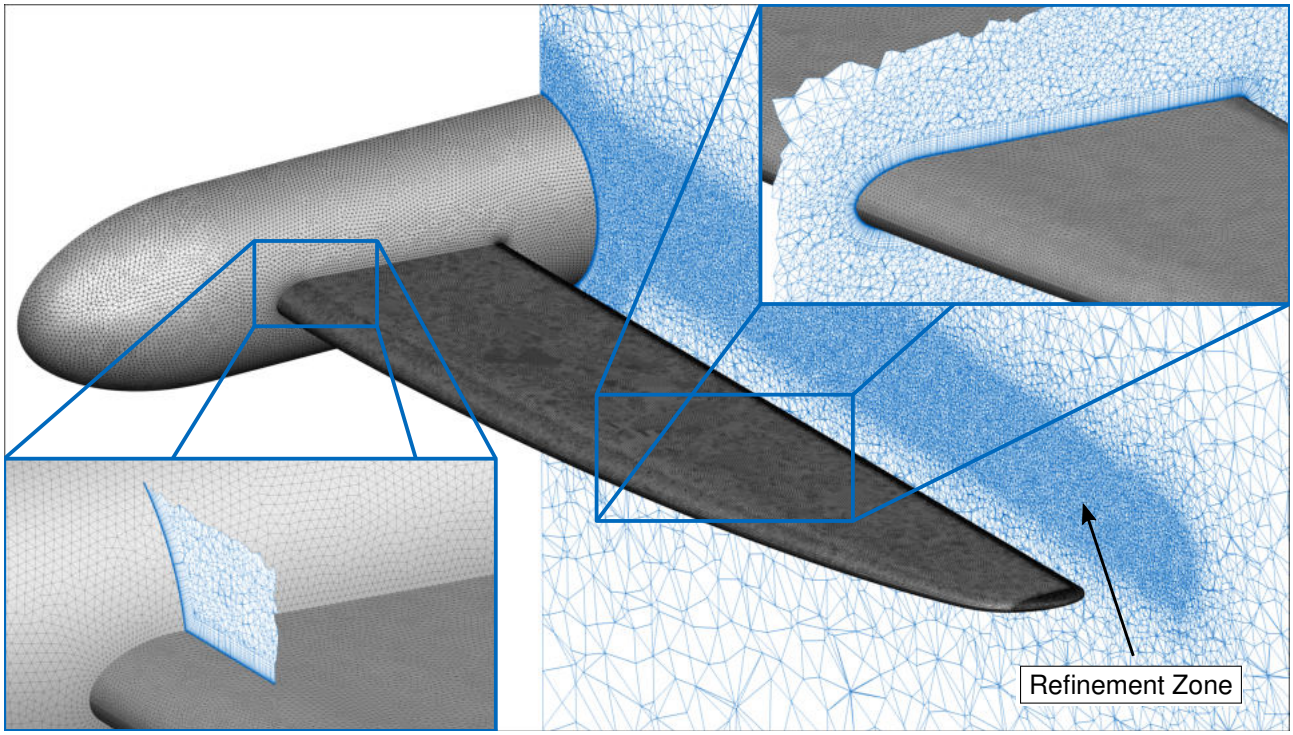

Figure 7 – Unstructured grid of the HAC with a detailed view of the prism-layer.

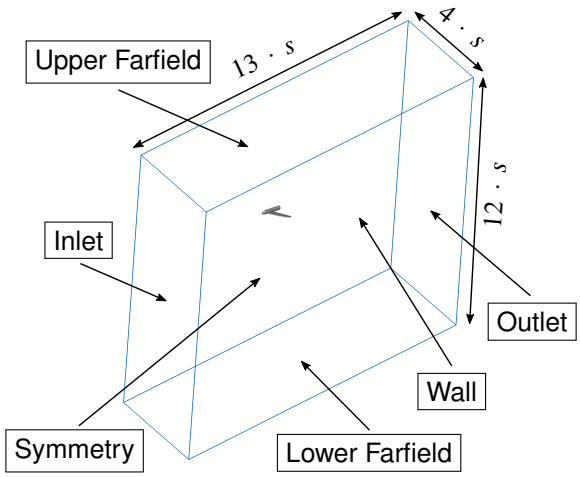

Figure 8 – Nomenclature and dimensions of the fluid domain depending on the half span s.

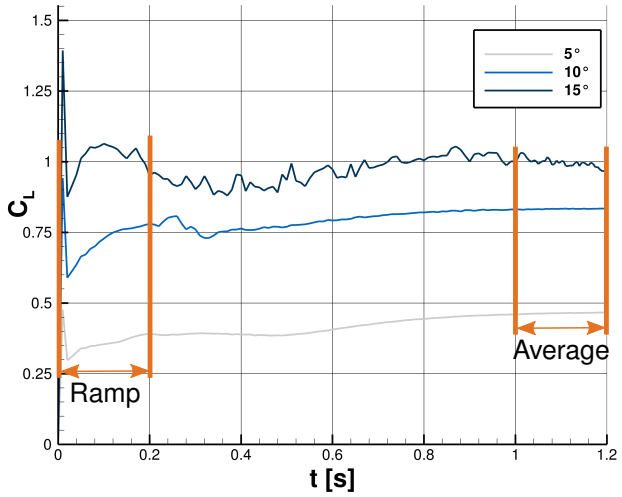

Figure 9 – Lift coefficient as a function of time for the HSC at $\alpha = [5°, 10°, 15°]$.

higher angles of attack, the numerical model shows less deformation on the top side, which could be a consequence of a more upstream located and larger area of flow separation.
At the HSC in Fig. 11, the discrepancies between experiment and simulation are bigger. On the top side, the location of the maximum deformation in the experiments is further upstream, and at $\alpha = 5°$ the amplitude becomes smaller. On the bottom side, the simulations lead to a less pronounced deformation, especially at $\alpha = 5°$. At higher angles of attack, the deformations agree better again.
Overall, the comparison shows a good agreement for the HAC and the HSC at the reference case of $\alpha = 10°$ and higher angles of attack. Nevertheless, for smaller angles of attack, the deformations of the numerical model deviate from the experimental data, which is also investigated by the aerodynamic coefficients in the next section.

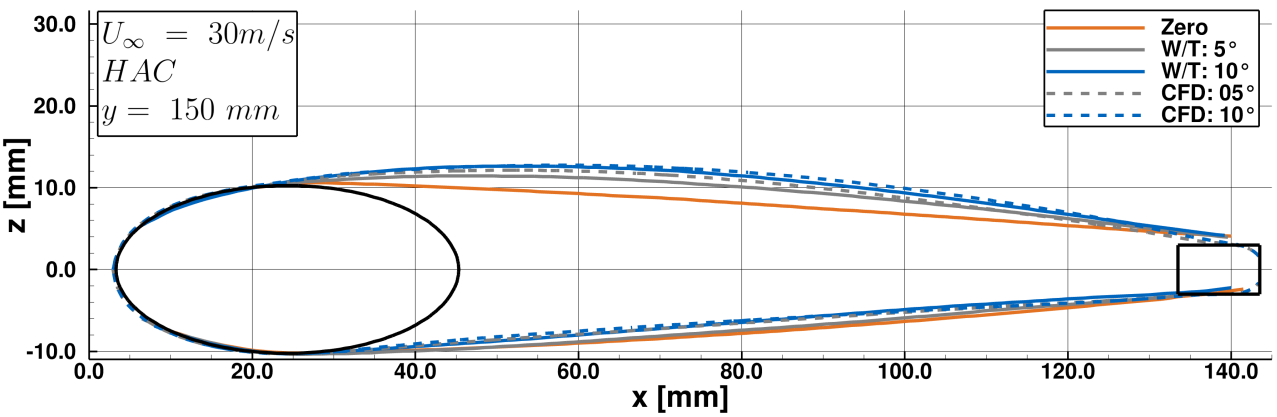

Figure 10 – Deformations at the cross section of the HAC at $y/s = 0.25$, $U_\infty = 30\ m/s$ and $\alpha = 5°, 10°$.

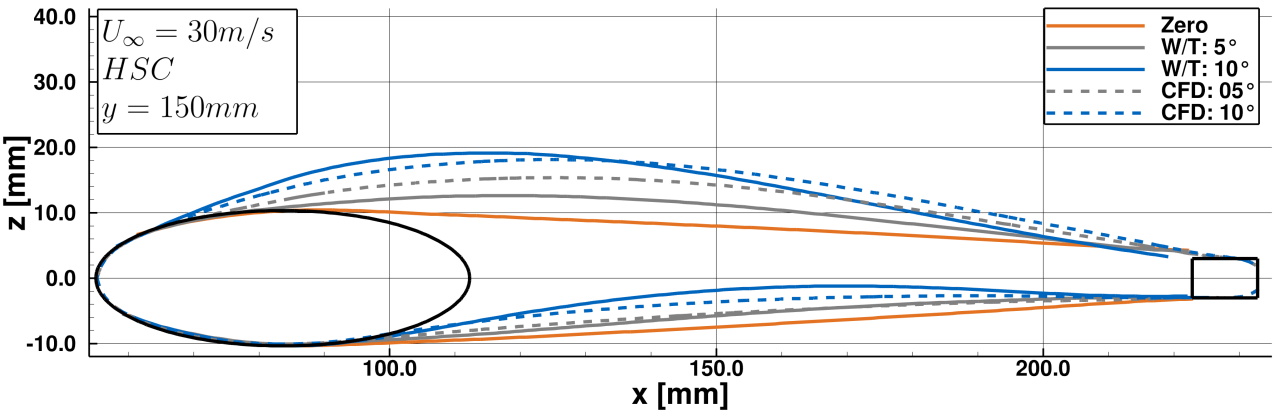

Figure 11 – Deformations at the cross section of the HSC at $y/s = 0.36$, $U_\infty = 30\ m/s$ and $\alpha = 5°, 10°$.

5.2 Aerodynamic Coefficients

In the following section, the lift coefficient C_L and the drag coefficient C_D are compared at $U_\infty = 30\ m/s$ for all three configurations. The resulting forces and moments from the numerical half model are made dimensionless by the dynamic pressure and the half wing surface. Figure 12 and Fig. 13 show the lift and drag coefficient as a function of the angle of attack. The experimental results are plotted as dotted lines and they are averaged over $5\ s$. The numerical results are shown as circles and are averaged over $0.2\ s$, as indicated in Fig. 9.
The lift coefficient of the experimental measurements shows a classical trend with a linear behavior for moderate angles of attack and a flattened region for high angles of attack. The gradient of the linear region rises with an increasing aspect ratios as expected. All configurations show a smooth

stall behavior, while the maximum lift coefficient $C_{L,max}$ is shifted to a higher angle of attack for the highly swept wings.
The simulated lift coefficient of the HSC indicates the best overall matching with a small positive offset. The numerical results of the HAC and the INT deviate from the experiments. At $\alpha = 5°$, the HAC shows the highest C_L, which indicates the steepest rise in the linear region. But both configurations reach their $C_{L,max}$ at smaller angles of attack than in the experiment, which is most likely linked to the flow separation behavior in the fluid simulations. In the numerical results of the HAC at $\alpha = 10°$, a large separation bubble is generated on the wing near the fuselage. Due to the design of the W/T model, the connection between the fuselage and the wing is less inclined than for the numerical model, which may contribute to a more downstream located flow separation. The lift polars of the numerical results seem to be shifted towards higher angles of attack, compared to the experimental curves. Further simulations, especially in the high-lift region, will show the behavior of the wing in more detail. At $\alpha = 5°$, the drag coefficient of the experiments and the simulations conforms for all three configurations. With an increasing angle of attack, the simulations show increased drag, which can be associated to larger areas of flow separation on the wing.

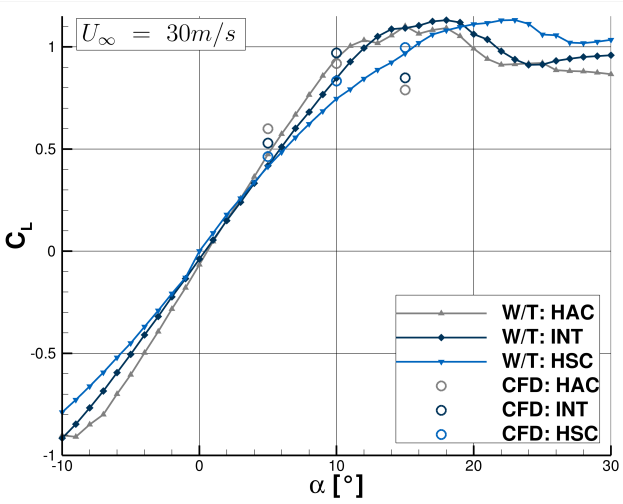

Figure 12 – Effects of different wing positions on the lift coefficient C_L as a function of the angle of attack α at $R_\infty = 264000$.

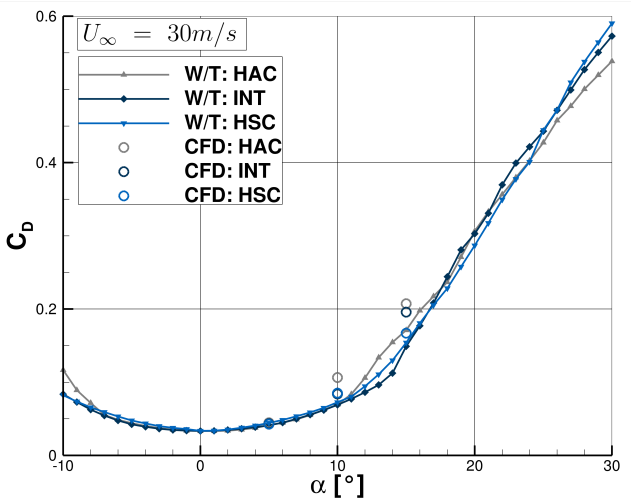

Figure 13 – Effects of different wing positions on the drag coefficient C_D as a function of the angle of attack α at $R_\infty = 264000$.

5.3 Flow Field

The wake flow field structures of the numerical simulations are compared to the ones of the stereo-PIV measurements. The experimental results are averaged over 400 images, while the numerical results are averaged over the last $0.2\ s$. Figure 14 shows the non-dimensional axial velocity distribution for all three configurations on slices $1.5 \times c_r$ downstream of the wing tip at $\alpha = 10°$, $U_\infty = 30\ m/s$, and $Re = 264000$. The experimental results are shown on the left and the numerical results on the right side. The TE is visualized in black and the slice positions are displayed in red on the sketches in the upper right corners.
The deep blue regions illustrate areas with smaller velocities than the free stream velocity. They indicate the position and the strength of the wing tip vortex as well as the shear layer behind the wing, which agree well between the experiments and the simulations. The small disturbance in the shear layer behind the HAC at $y = 0.48\ m$ does not occur in the numerical results, because the kink of the TE is neglected in the simulations. In addition, in the W/T the flow remains attached, while the simulations show a bubble with decelerated flow close to the fuselage on the right edge.
At the HSC, the initially in the W/T results observed warps or wrinkles, respectively, of the shear layer can also be found in the numerical results. By a detailed view into the flow field of the numerical results, the source of the warping and wrinkling structures can be identified as small vortices sepa-

rating from the LE and the roll-up process of the shear layer behind the wing. The increasing sweep in spanwise direction leads to multiple small LE vortices with respect to the associated changes in the spanwise circulation gradient, which separate shortly after their formation. At the TE, the shear layer interacts with the vortices and coils up around them.
In Fig. 15, the wake of the wing is compared for the experimental and the numerical results by plots of the non-dimensional axial vorticity. The blue regions with a high absolute vorticity indicate the wing tip vortex and the shear layer behind the wing. At the HAC, the separation bubble is visible by the red area with a positive vorticity. The shear layer warping occurs at the HSC and the INT.

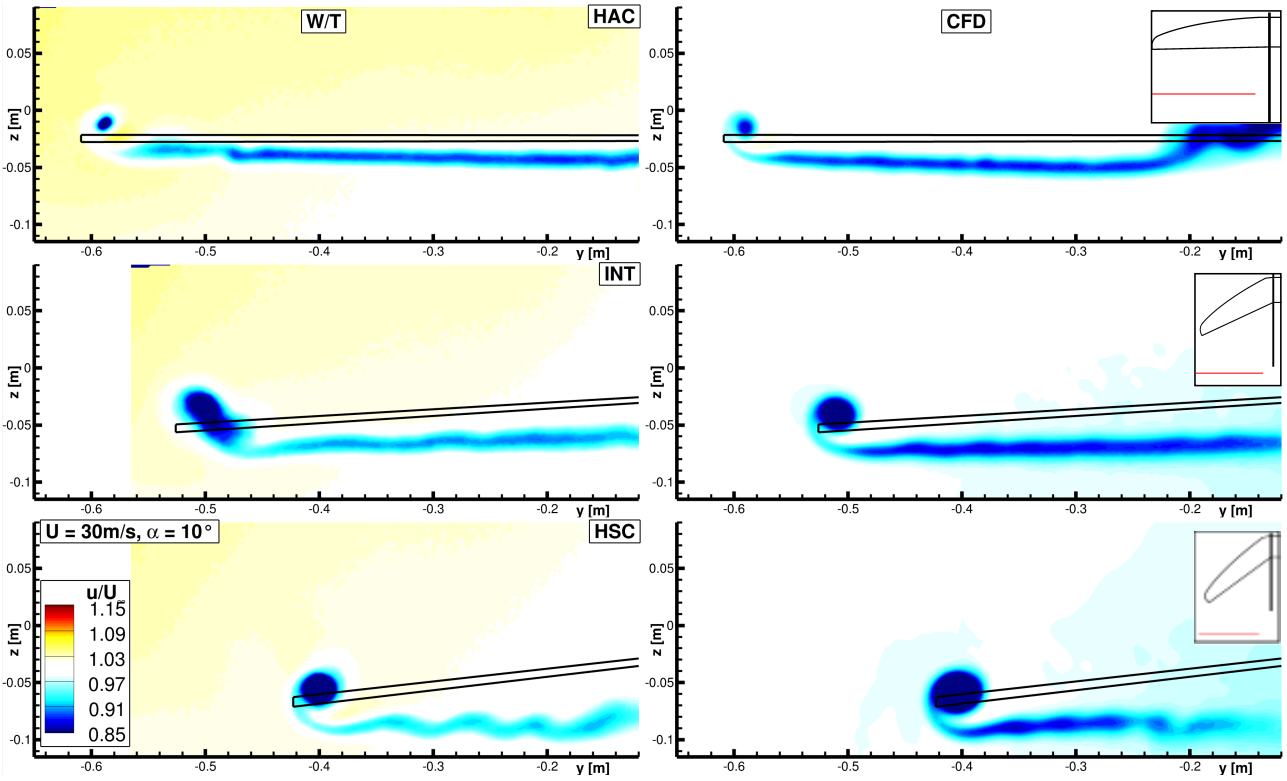

Figure 14 – The non-dimensional axial velocity field u/U_∞ at $1.5 \times c_r$ downstream of the wing tip at $U_\infty = 30\ m/s$ for $\Omega = [23°, 43°, 63°]$ and $\alpha = 10°$.

6. Conclusion and Outlook

Fluid-structure-interaction simulations of an elasto-flexible membrane wing are performed at a Reynolds number of 264000. Three angles of attack $\alpha = [5°, 10°, 15°]$ for three different folding angles, related to different wing sweeps and aspect ratios, $\Omega = [23°, 43°, 63°]$ are simulated. For validation, the numerical simulations are compared with experimental results. Hereby, the membrane deformation, the aerodynamic coefficients and the wake flow field of the wing are examined.
The numerical results of the highly swept wing agree well with the experimental data. With a more extended wing, the lift is overpredicted for small angles of attack, which is due to an excessive deformation of the membrane and thus insufficient pre-stress. The maximum lift coefficient of the intermediate and the high aspect ratio configuration is reached at lower angles of attack, which can be explained by the critical flow separation behavior. Overall, the lift polars of the numerical results seem to be shifted towards higher angles of attack, compared to the experimental curves. The influence of the mesh, small deviations of the geometry and other numerical settings will be investigated in more detail.

Acknowledgement The project is funded by the Deutsche Forschungsgemeinschaft (DFG, German Research Foundation) grant number BR 1511/12-1.

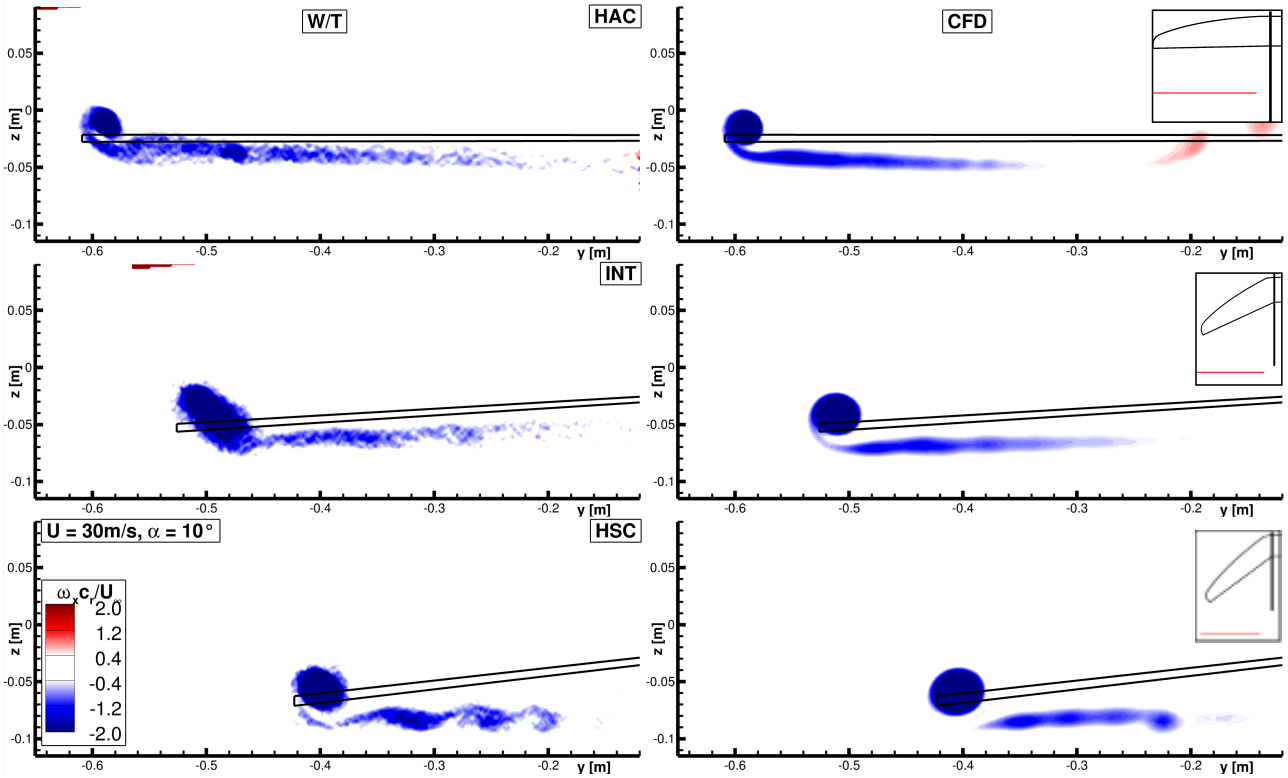

Figure 15 – The non-dimensional axial vorticity field $\omega_x \cdot c_r/U_\infty$ at $1.5 \times c_r$ downstream of the wing tip at $U_\infty = 30\ m/s$ for $\Omega = [23°, 43°, 63°]$ and $\alpha = 10°$.

7. Contact Author Email Address

mailto: jonathan.pflueger@tum.de

8. Copyright Statement

References

[1] Ifju P, Waszak M and Jenkins L. Stability and control properties of an aeroelastic fixed wing micro aerial vehicle. *AIAA Atmospheric Flight Mechanics Conference and Exhibit*, Montreal, 2001.

[2] Moorhouse D, Sanders B, Spakovsky M, Butt J. Benefits and design challenges of adaptive structures for morphing aircraft. *The Aeronautical Journal*,Vol. 110, No. 1105, pp. 157-162, 2006.

[3] Vasista S, Tong L, Wong KC. Realization of Morphing Wings: A Multidisciplinary Challenge. *Journal of Aircraft*, Vol. 49. No. 1, pp. 11–28, 2012.

[4] Jenkins D, Ifju P, Abdulrahim M and Olipra. Assessment of Controllability of Micro Air Vehicles. 2011.

[5] Song A, Tian X, Israeli E, Galvao R, Bishop K, Swartz S, Breuer K. Aeromechanics of Membrane Wings with Implications for Animal Flight. *AIAA Journal*, Vol. 46, No. 8, pp. 2096-2106, 2008.

[6] Piquee J, Breitsamter C. Numerical and Experimental Investigations of an Elasto-Flexible Membrane Wing at a Reynolds Number of 280000. *Aerospace*, Vol. 4, No. 39, 2017.

[7] Béguin B. *Development and Analysis of an Elasto-flexible Morphing Wing.* PhD Thesis, Technical University of Munich, 2014.

[8] He X, Guo Q, Wang J. Extended flexible trailing-edge on the flow structures of an airfoil at high angle of attack. *Experiments in Fluids*, Vol. 60, No. 8, 2019.

[9] Guo Q, He X, Wang Z, Wang J. Effects of wing flexibility on the aerodynamic performance of an aircraft model. *Chinese Journal of Aeronautics*, in press.

[10] Béguin B, Breitsamter C. Effects of membrane pre-stress on the aerodynamic characteristics of an elasto-flexible morphing wing. *Aerospace Science and Technology*, Vol. 37, pp. 138–150, 2014.

[11] Breuer K, Swartz S, Peraire J, Drela M, Willis D, Moss C, Batten B. Biologically-Inspired Flight for Micro Air Vehicles. Final Report, Brown University, School of Engineering, Providence, 2012.

[12] Wilkinson M.T. Sailing the skies: The improbable aeronautical success of the pterosaurs. *Journal of Experimental Biology*, Vol. 210, pp. 1663-1671, Cambridge, 2007.

[13] Wieneke B. PIV uncertainty quantification from correlation statistics. *Measurement Science and Technology*, Vol. 26, No. 7, 2015.

[14] Pflueger J, Breitsamter C. Experimental Investigations of a Full Model with Adaptive Elasto-Flexible Membrane Wings. *Chinese Journal of Aeronautics*, Vol. 34, No. 7, pp. 211-218, 2020.

[15] Pflueger J, Breitsamter C. Deformation Measurements of a Full Span Model with Adaptive Elasto-Flexible Membrane Wings. *New Results in Numerical and Experimental Fluid Mechanics XIII*, Contributions to the 22nd STAB/DGLR Symposium, 2022.

[16] Bayerischen Akademie der Wissenschaften, Linux-Cluster am Leibniz-Rechenzentrum, https://doku.lrz.de/display/PUBLIC/Linux+Cluster, 2021.

[17] ANSYS, Inc. System Coupling User's Guid. 2020.